SUPPORTING INFORMATION

Phosphine-Functionalized Amidinate Ligated Rare-Earth Metal Complexes for Highly 3,4-Selective Living Polymerization of 1,3-Conjugated Dienes

Fen You,[a] Jixing Wang,[a] Hui Liu,[a] Xiaohui Kang,[b]* Xiaochao Shi[a]*

a. Department of Polymer Materials, School of Materials Science and Engineering, Shanghai University, Materials Building, Nanchen Street 333, Shanghai 200444, China.

b. College of Pharmacy, Dalian Medical University, Dalian 116044, China

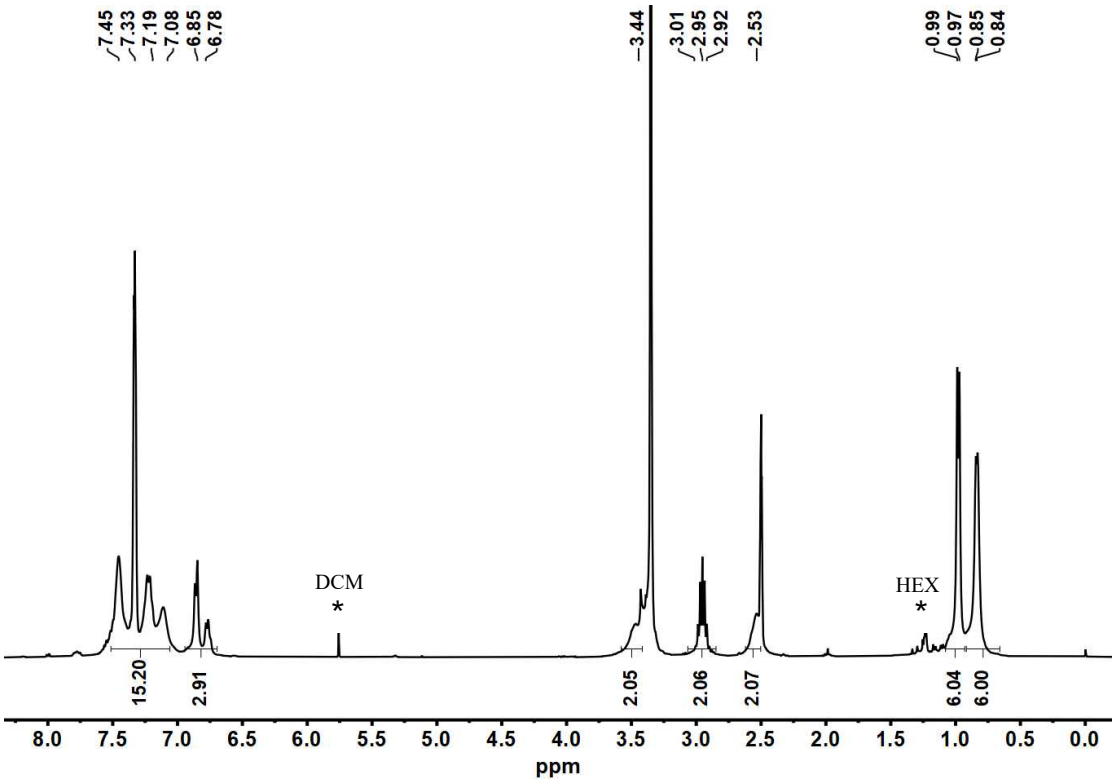

Figure S1. ^{1}H NMR spectrum of ligand **L1-H** in DMSO-d_6 at 25 °C

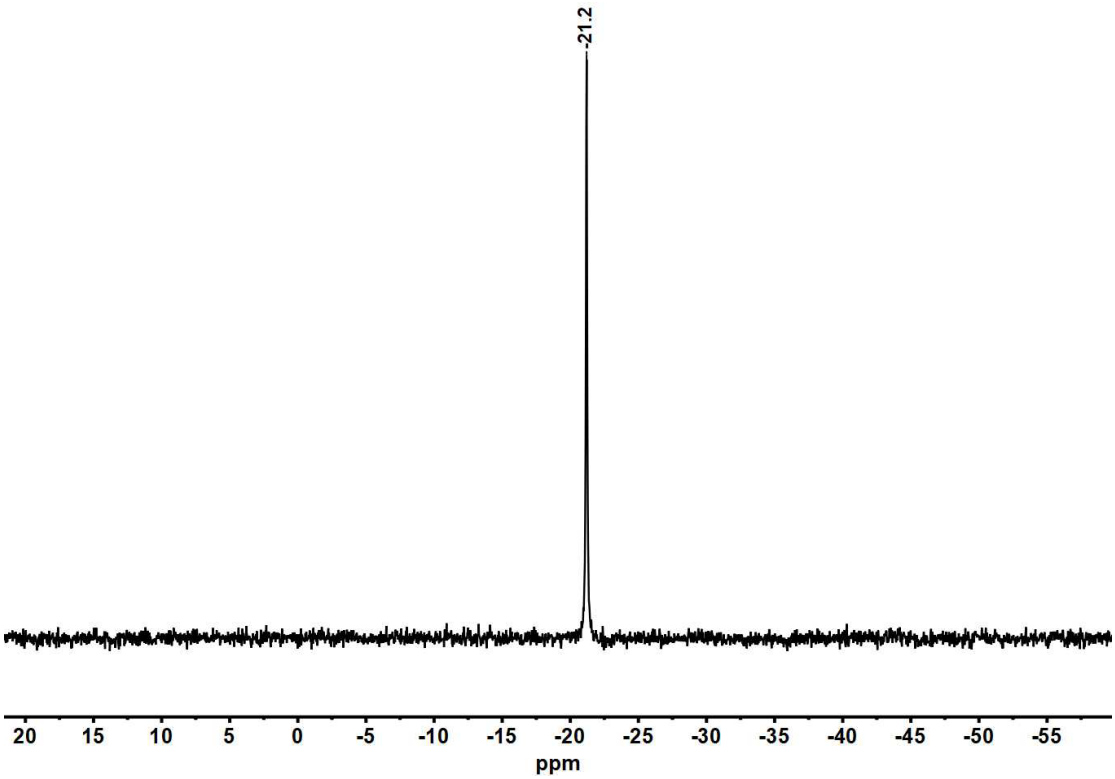

Figure S2. ^{31}P NMR spectrum of ligand **L1-H** in DMSO-d_6 at 25 °C.

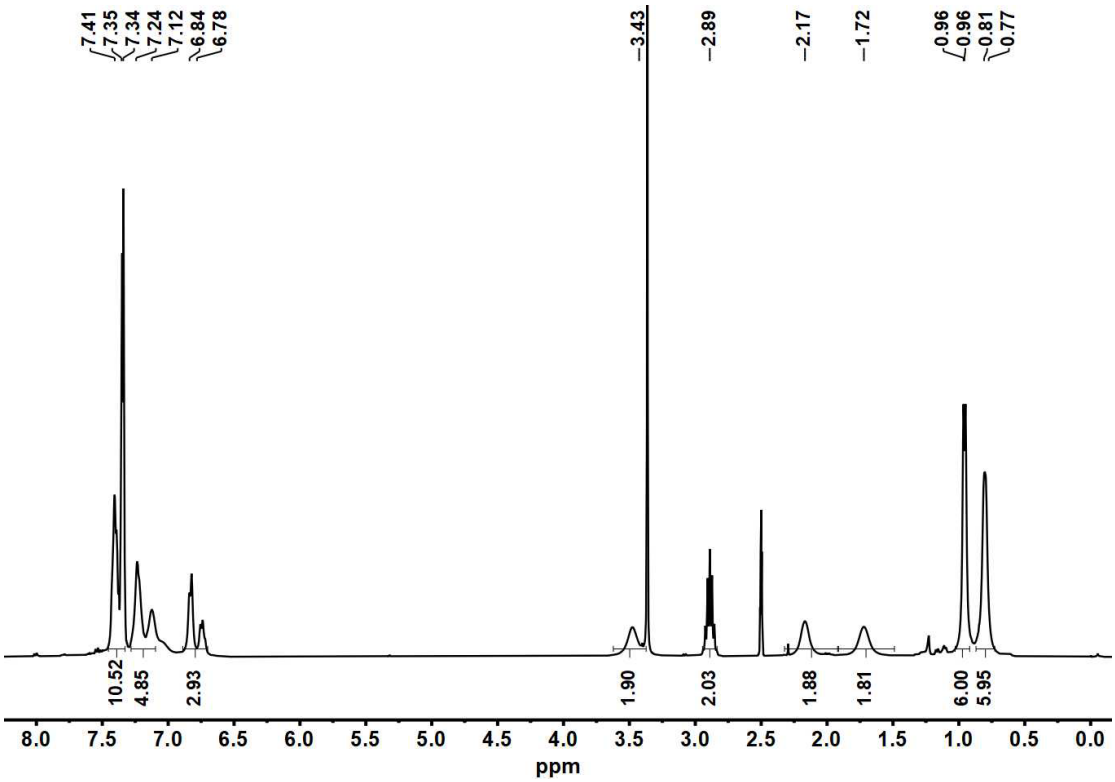

Figure S3. ^{1}H NMR spectrum of ligand **L2-H** in DMSO-d_6 at 25 °C

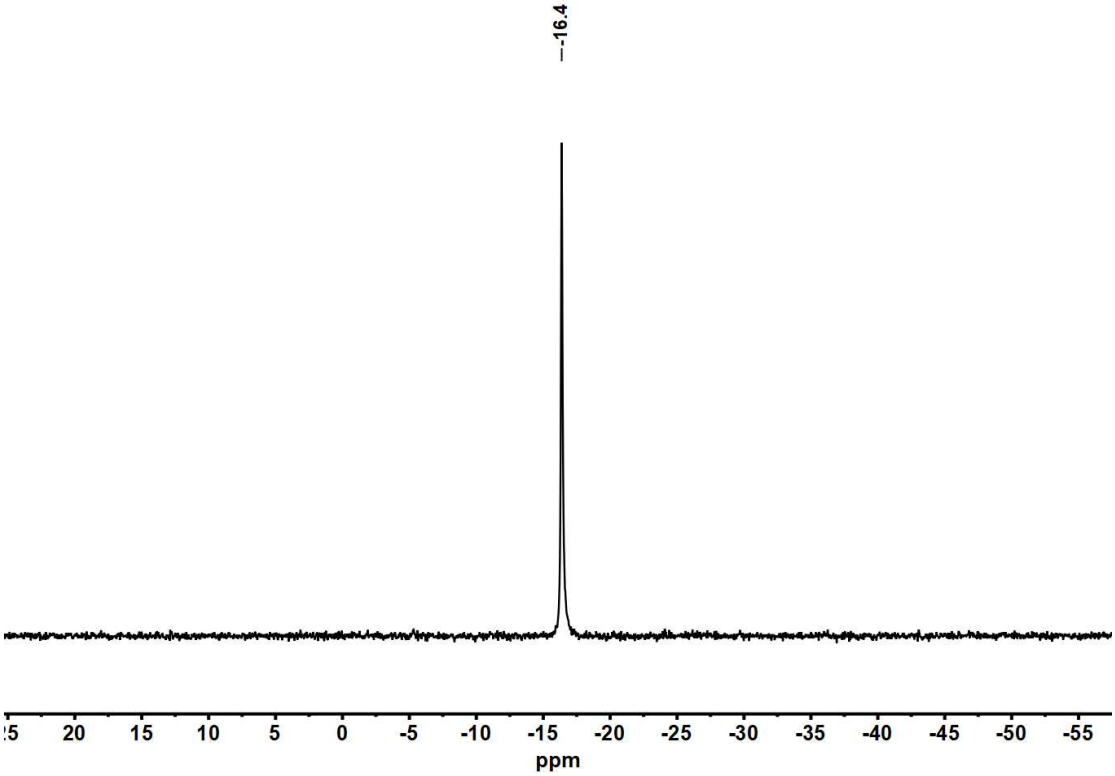

Figure S4. ^{31}P NMR spectrum of ligand **L2-H** in DMSO-d_6 at 25 °C.

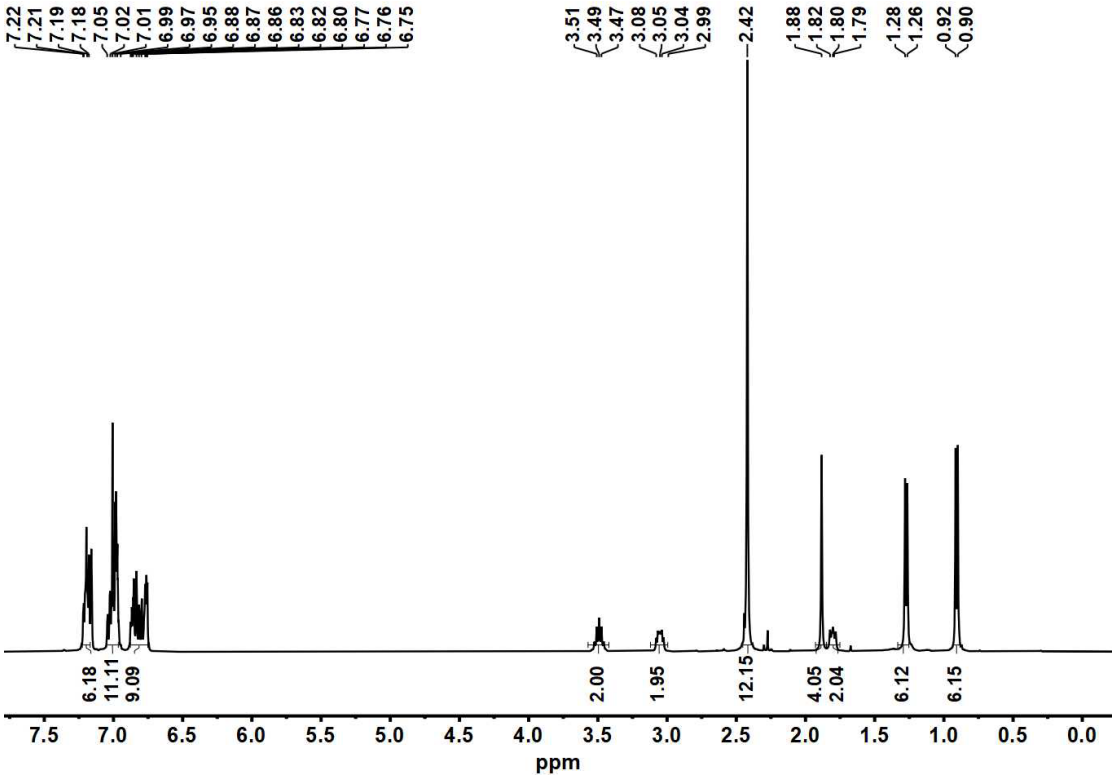

Figure S5. ^{1}H NMR spectrum of complex **P1-Sc** in C_6D_6 at 25 ºC

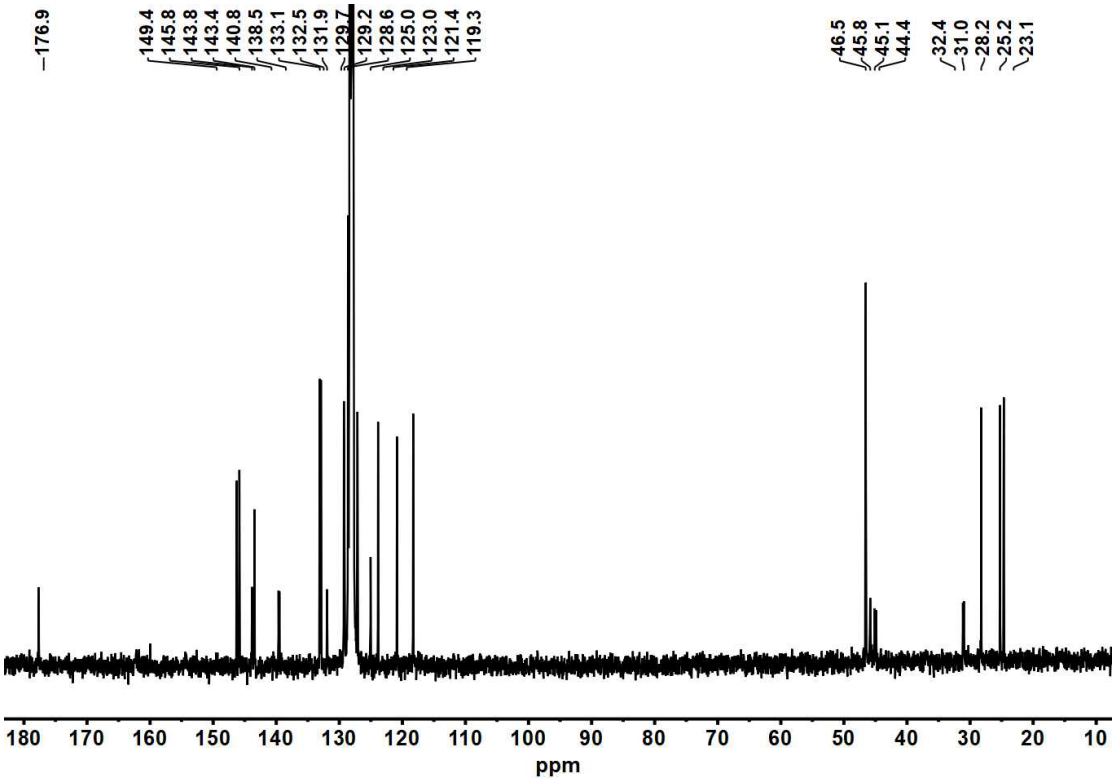

Figure S6. ^{13}C NMR spectrum of complex **P1-Sc** in C_6D_6 at 25 ºC

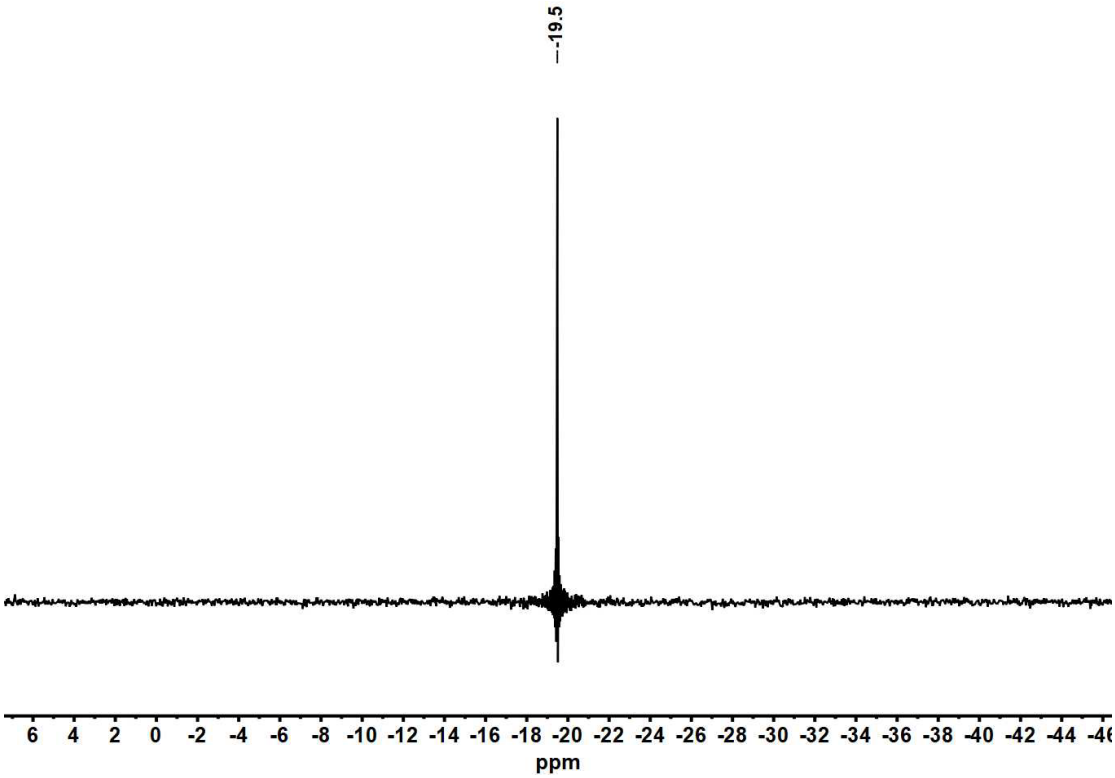

Figure S7. ^{31}P NMR spectrum of complex **P1-Sc** in C_6D_6 at 25 °C

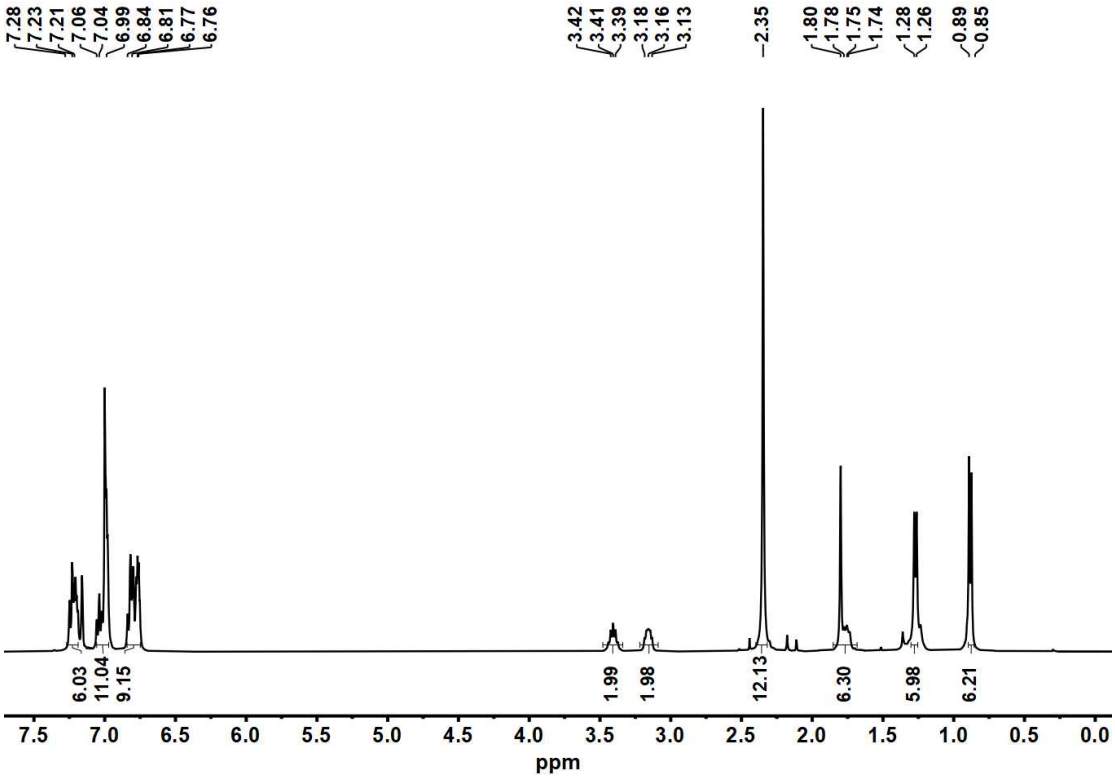

Figure S8. ^{1}H NMR spectrum of complex **P1-Lu** in C_6D_6 at 25 °C

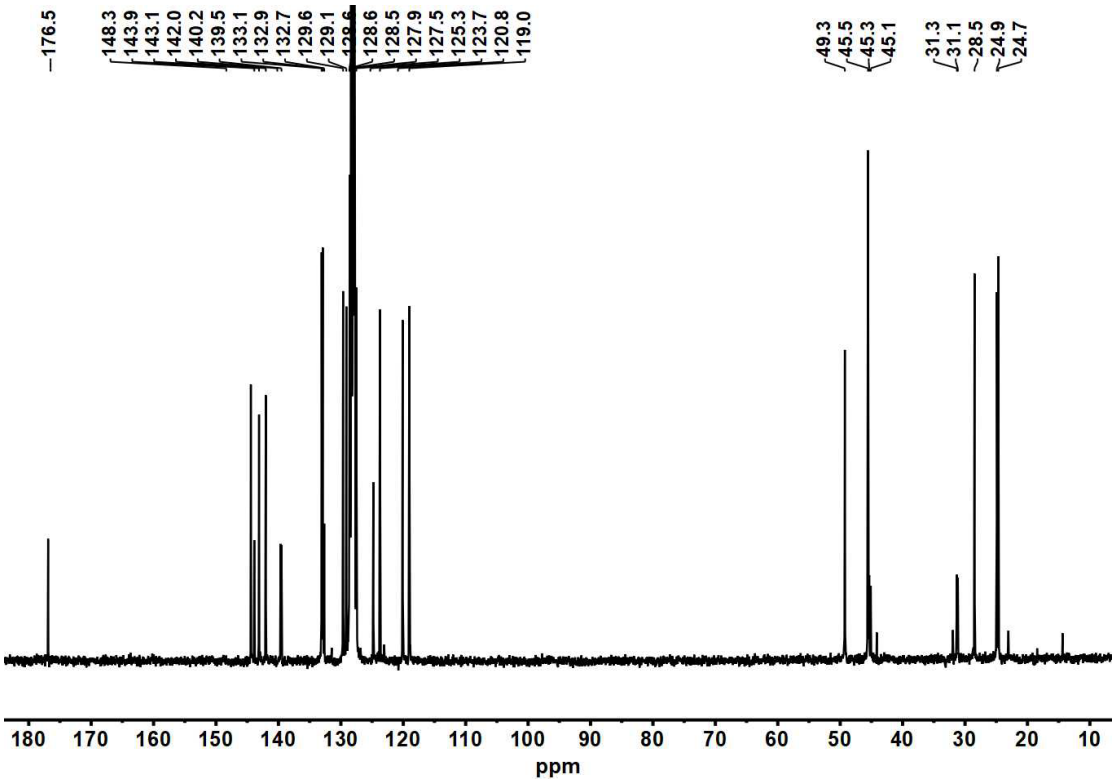

Figure S9. ^{13}C NMR spectrum of complex **P1-Lu** in C_6D_6 at 25 °C

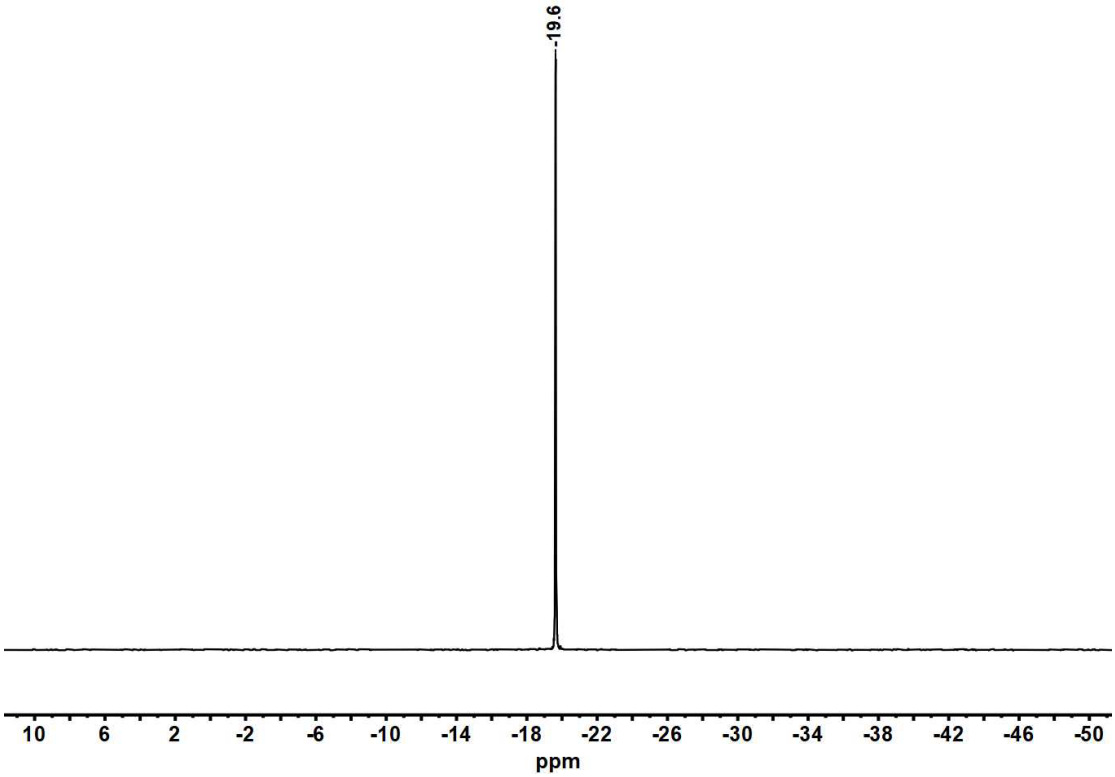

Figure S10. ^{31}P NMR spectrum of complex **P1-Lu** in C_6D_6 at 25 °C

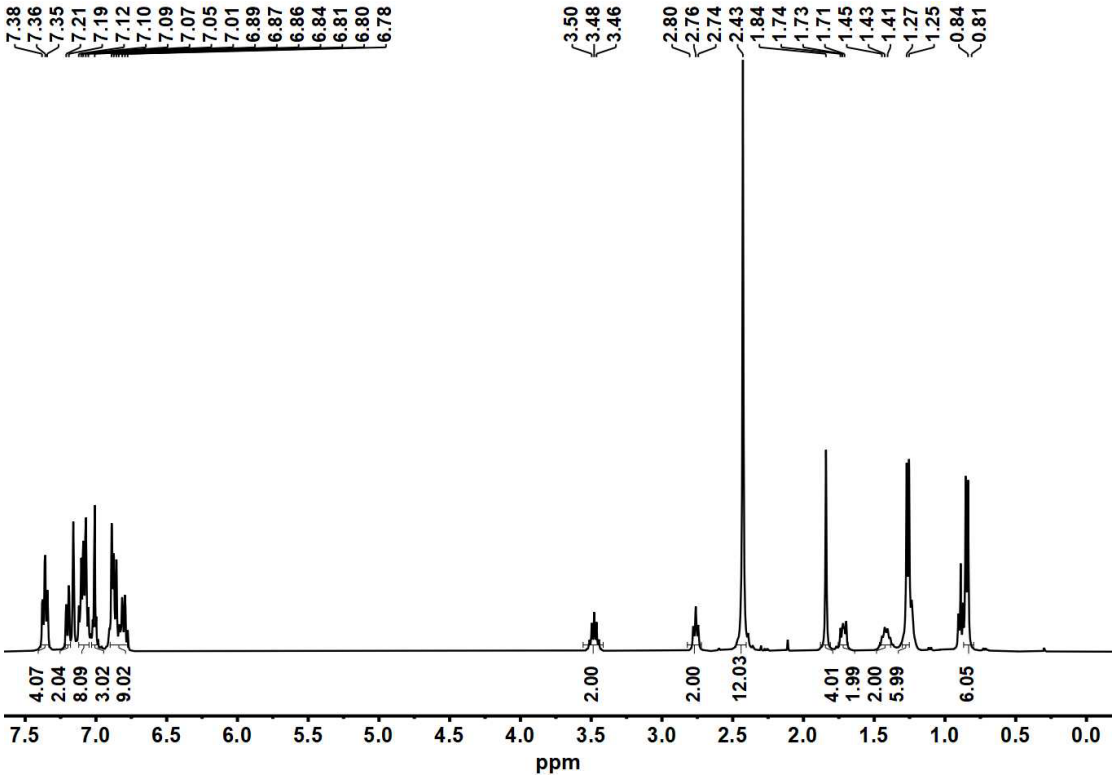

Figure S11. ^{1}H NMR spectrum of complex **P2-Sc** in C_6D_6 at 25 °C

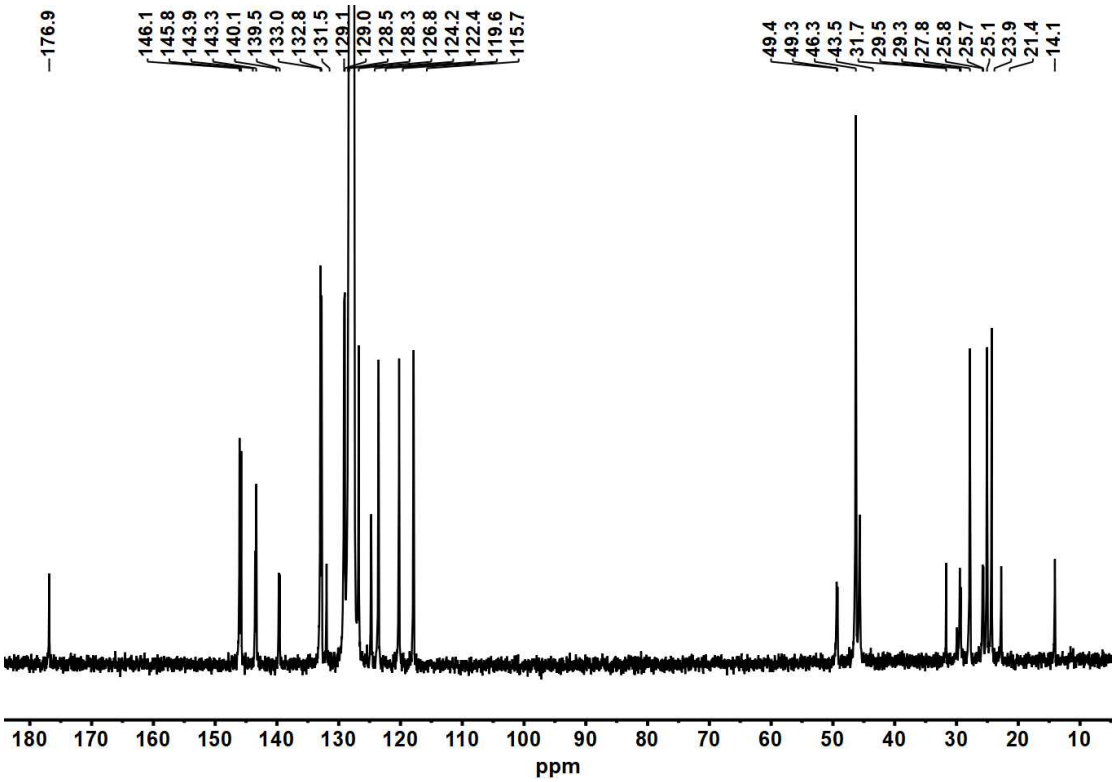

Figure S12. ^{13}C NMR spectrum of complex **P2-Sc** in C_6D_6 at 25 °C

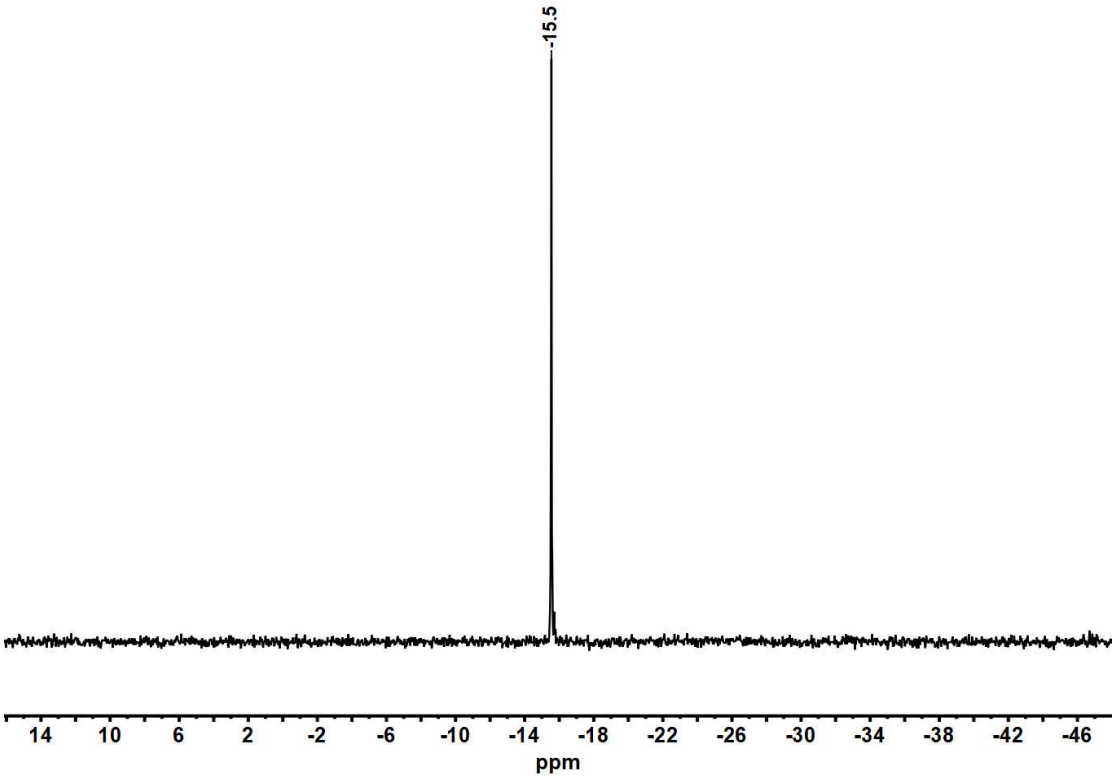

Figure S13. ^{31}P NMR spectrum of complex **P2-Sc** in C_6D_6 at 25 °C

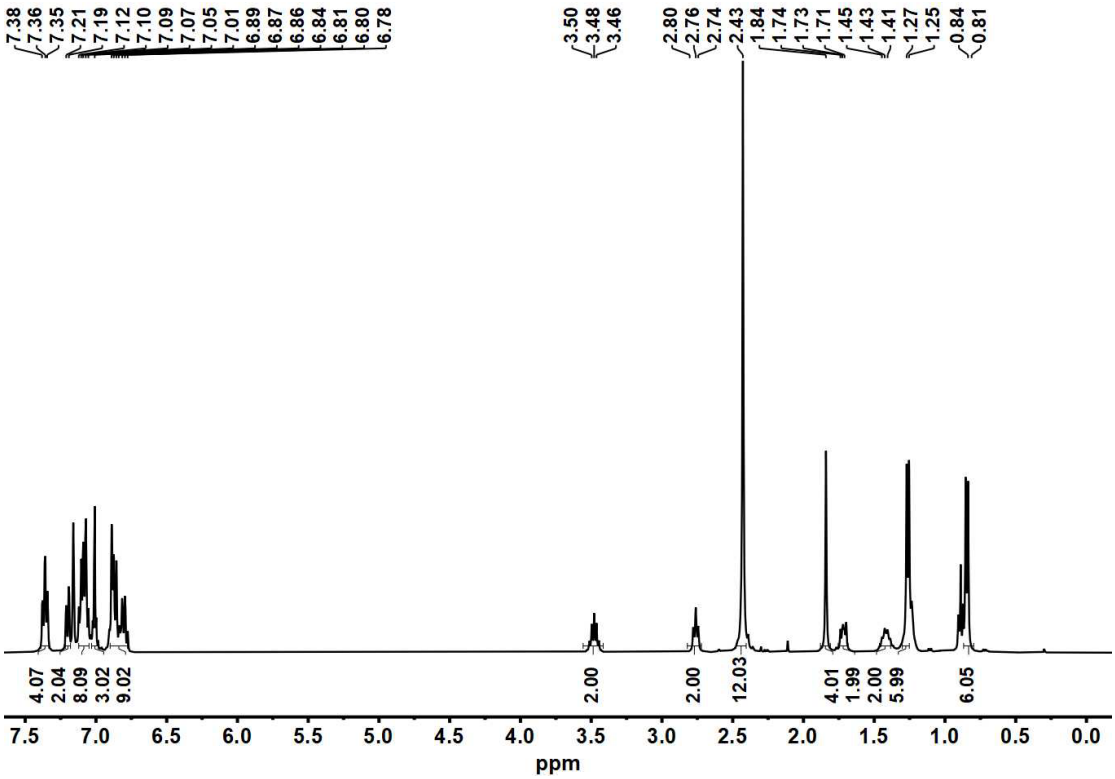

Figure S14. ^{1}H NMR spectrum of complex **P2-Lu** in C_6D_6 at 25 °C

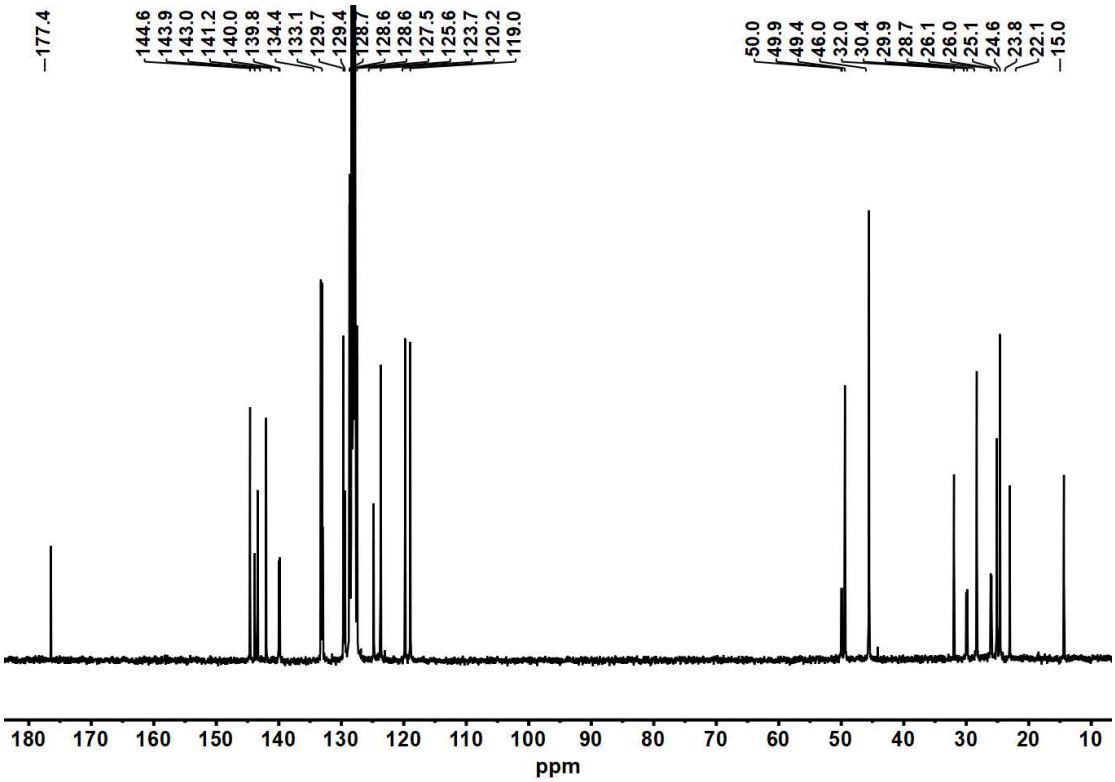

Figure S15. ^{13}C NMR spectrum of complex **P2-Lu** in C_6D_6 at 25 °C

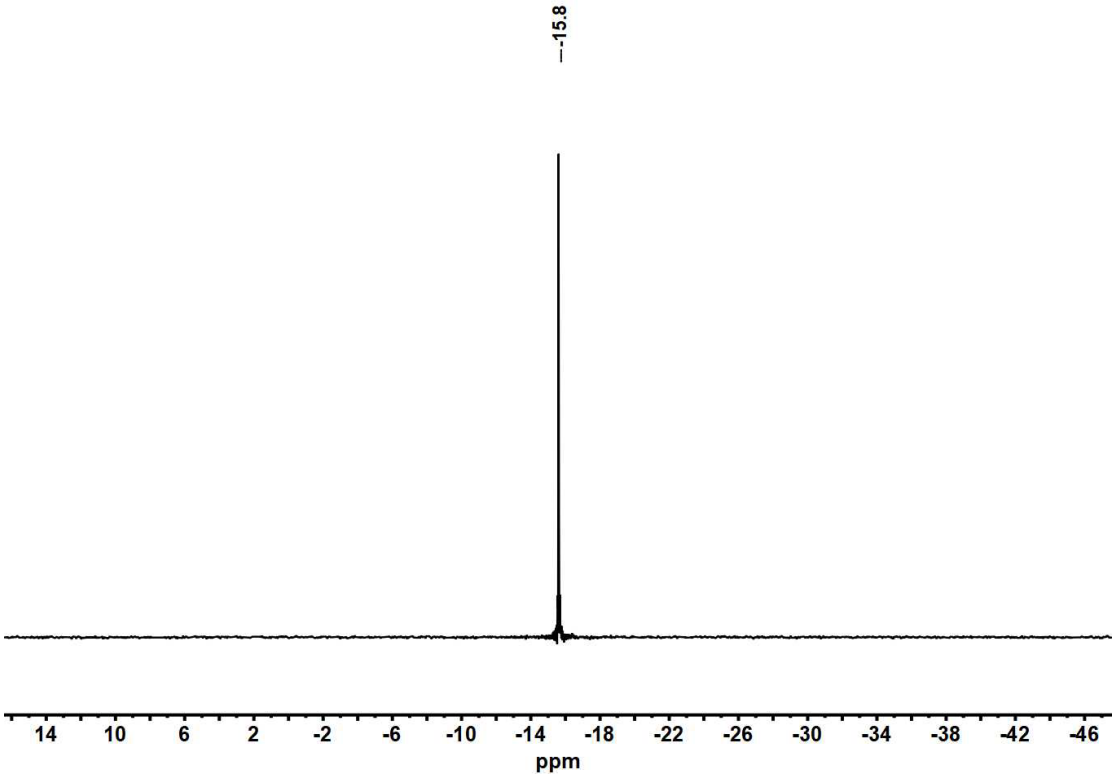

Figure S16. ^{31}P NMR spectrum of complex **P2-Lu** in C_6D_6 at 25 °C

Table S1. Polymerization of isoprene with complexes based on phosphine-functionalized amidinated ligands.

Entry	Cat	[M]/[cat]	T/°C	t/min	Con/%	Act/kg mol^{-1} h^{-1}	microstructure[b] 3,4-	M_n[c]	M_w/M_n[c]	*Eff*/%
1	**P1-Lu**	500	25	3	100	≥609	96.9	4.6	1.09	74.0
2	**P1-Lu**	1000	25	10	100	≥204	96.7	9.1	1.48	74.9
3	**P2-Sc**	500	25	30	34	23.2	99.3	7.8	1.45	14.8
4	**P2-Sc**	1000	25	200	100	≥20.4	99.0	44.8	1.13	15.2
5	**P2-Lu**	500	25	5	95	388	97.1	9.7	1.23	33.3
6	**P2-Lu**	1000	25	15	100	≥272	96.9	18.9	1.36	36.0

[a]Conditions: toluene (6 mL); catalyst (20 μmol); [Ln] / Co-cat. = 1:1 Co-cat. = $[Ph_3C][B(C_6F_5)_4]$. [b]Measured by means of ^{1}H NMR and ^{13}C NMR spectroscopy in $CDCl_3$. [c]Determined by gel permeation chromatography (GPC) against polystyrene standards at 35 °C. M_n in the unit of 10^4 g mol^{-1}.

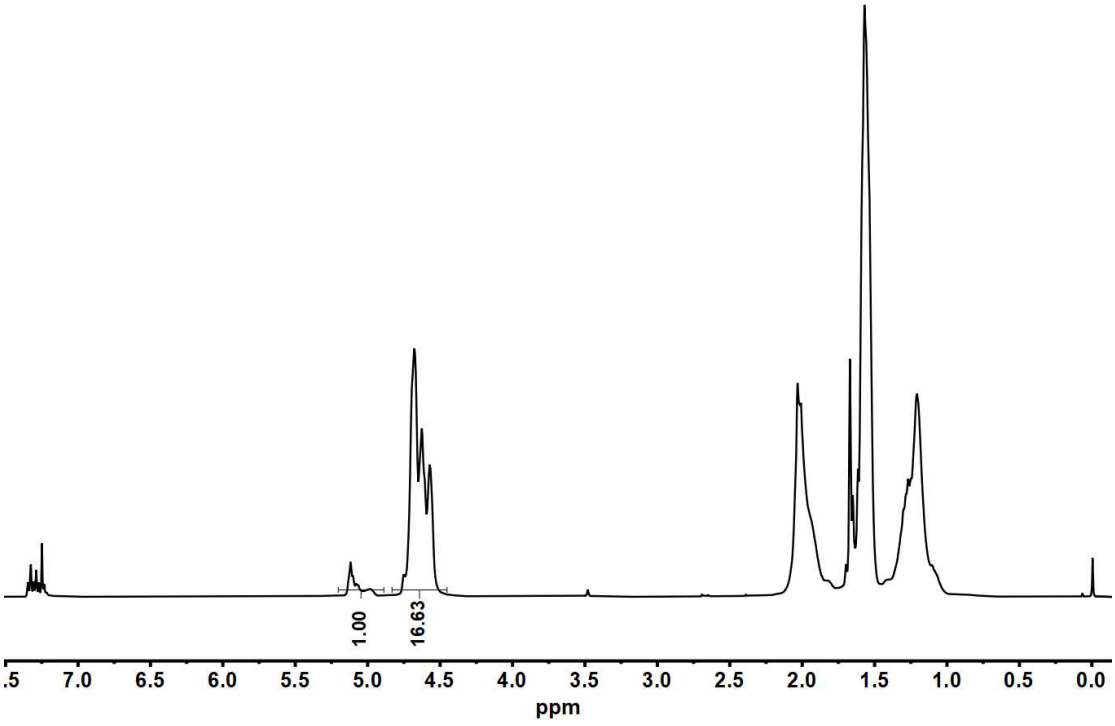

Figure S17. ^{1}H NMR (400M, $CDCl_3$, 25 °C) of Polyisoprene sample. (Entry 14, Table 1)

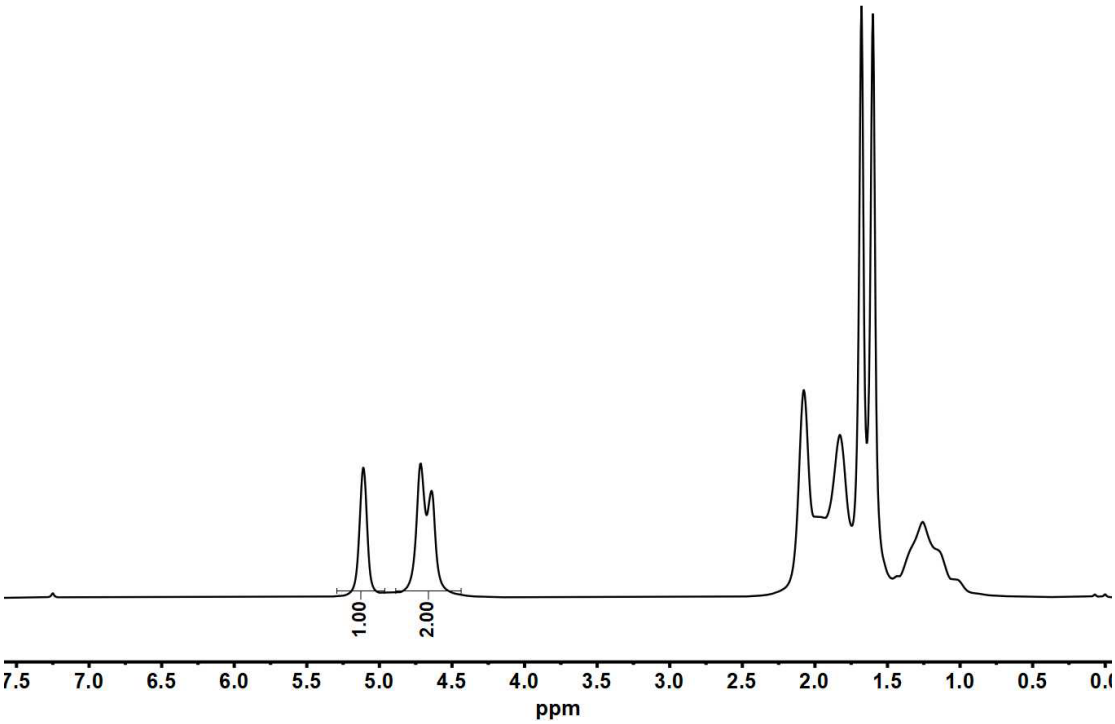

Figure S18. ^{1}H NMR (400M, $CDCl_3$, 25 °C) of Polymyrcene sample. (Entry 1, Table 2)

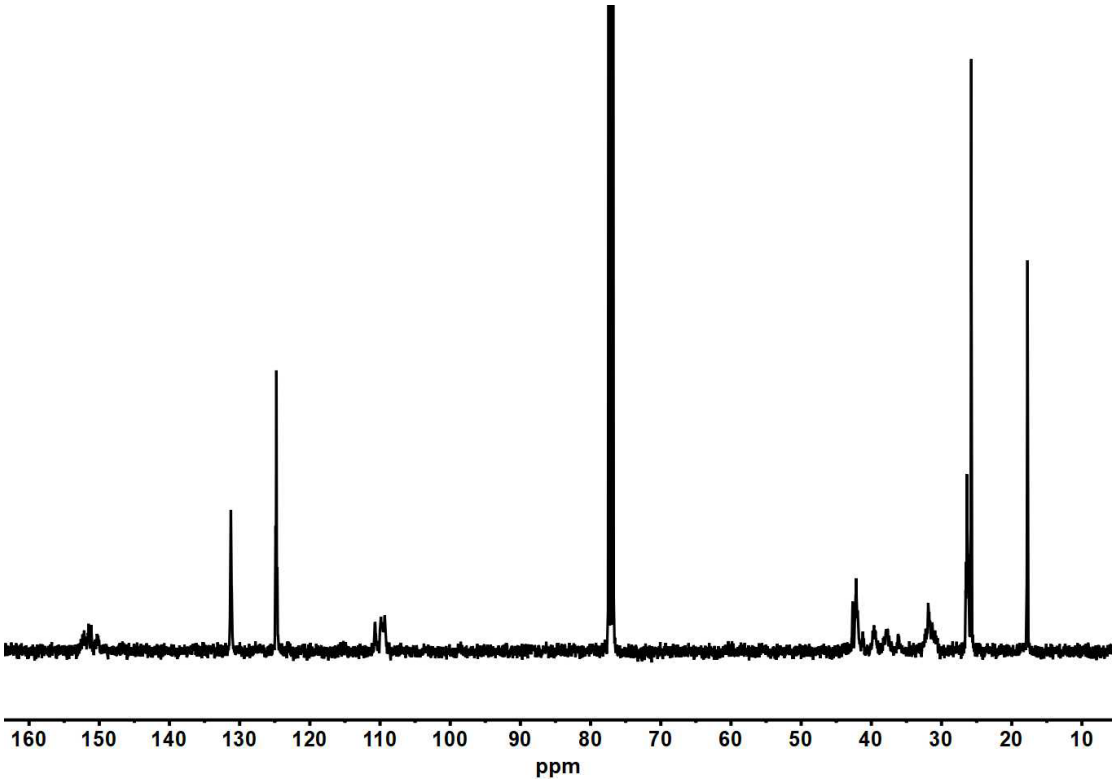

Figure S19. ^{13}C NMR (400M, $CDCl_3$, 25 °C) of Polymyrcene sample. (Entry 1, Table 2)

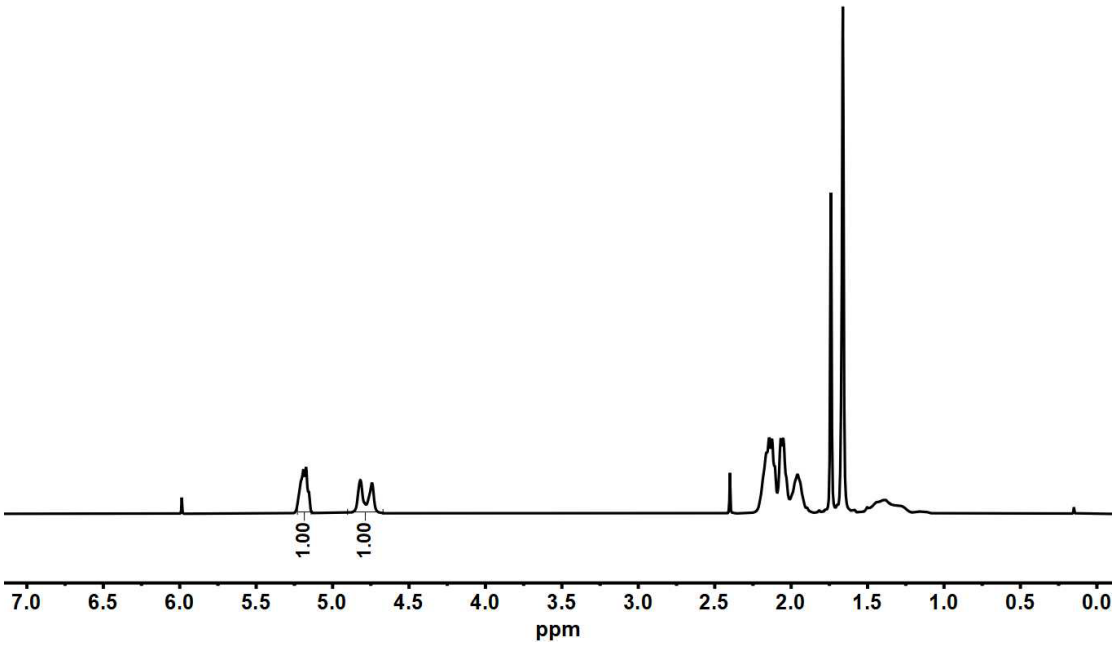

Figure S20. ^{1}H NMR (400M, $C_2D_2Cl_4$, 120 °C) of Polyfarnesene sample. (Entry 5, Table 2)

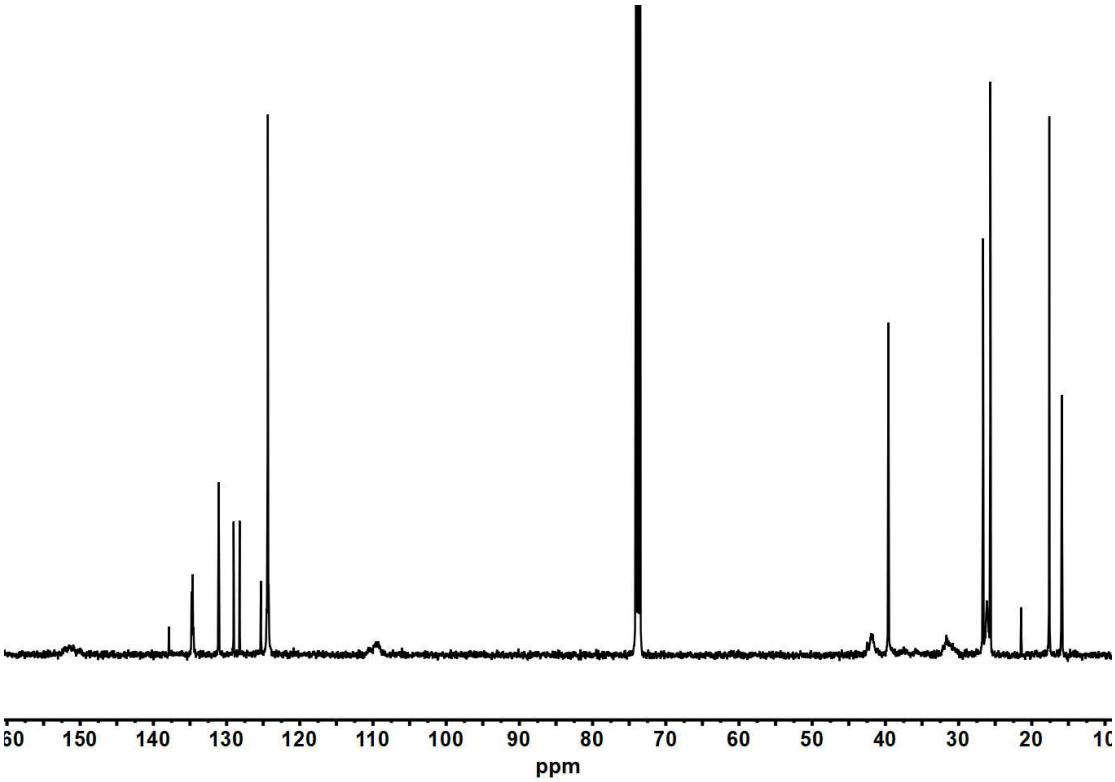

Figure S21. ^{13}C NMR (400M, $C_2D_2Cl_4$, 25 °C) of Polyfarnesene sample. (Entry 5, Table 2)

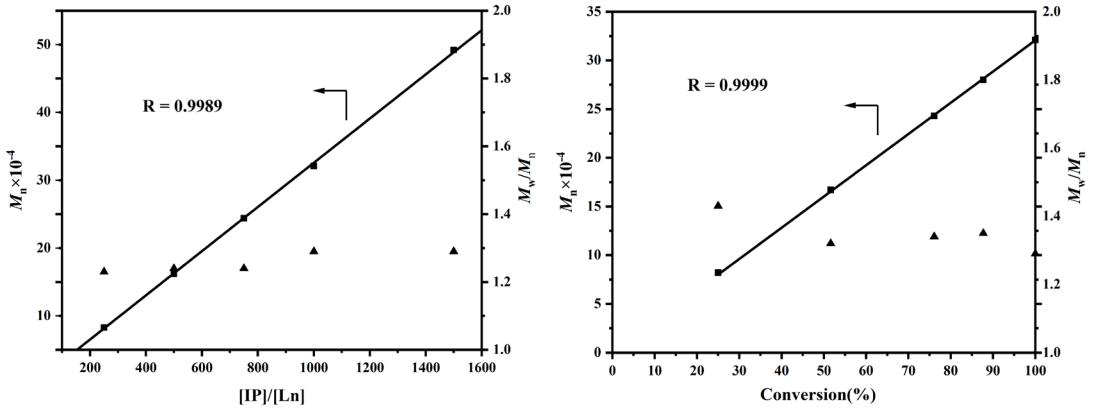

Figure S22. Plot of the polyisoprene M_n and PDI (M_w/M_n) as a function of [IP]/[Ln]. (left; Entries 2, 5-8, Table 1). Plot of the polyisoprene M_n and PDI (M_w/M_n) as a function of conversion. (right; Entries 7, 9-12, Table 1). With use of **P1-Sc**/[Ph_3C][$B(C_6F_5)_4$] as catalyst.

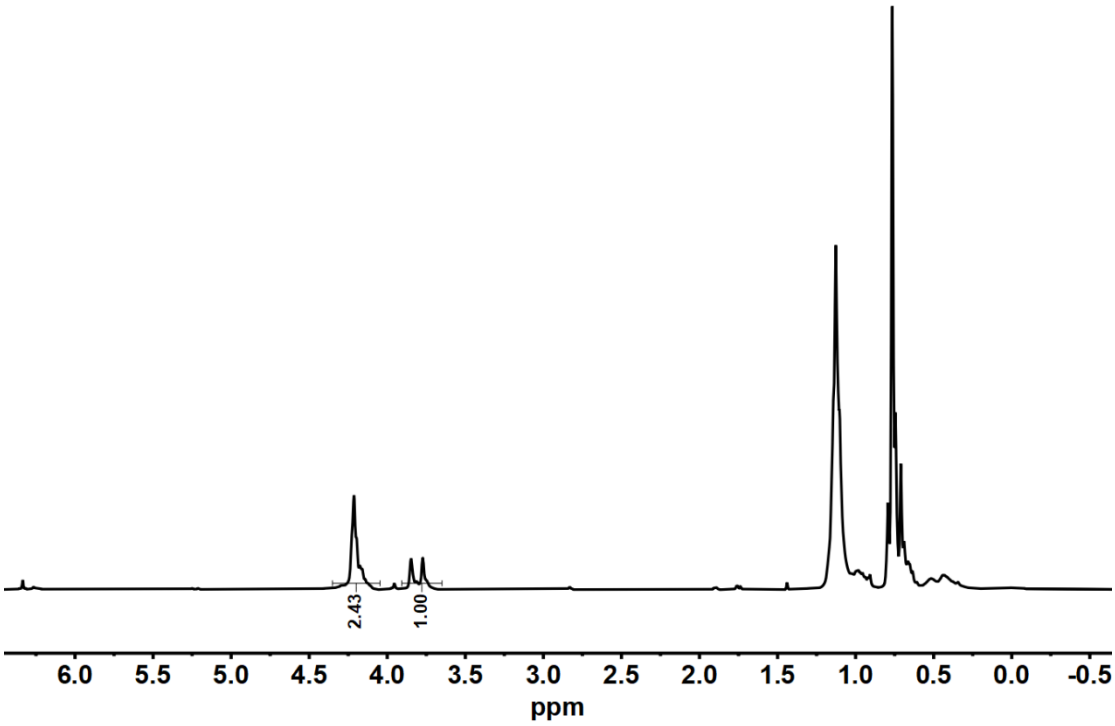

Figure S23. ^{1}H NMR (400M, $CDCl_3$, 25 °C) of Polyisoprene sample. (Sc($CH_2C_6H_4NMe_2$-*o*)$_3$/[Ph_3C][$B(C_6F_5)_4$] binary system)

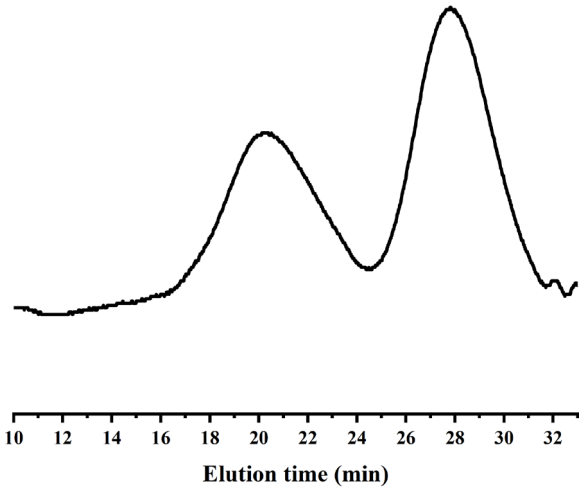

Figure S24. GPC curve of the polyisorene from $Sc(CH_2C_6H_4NMe_2\text{-}o)_3$/$[Ph_3C][B(C_6F_5)_4]$ binary system

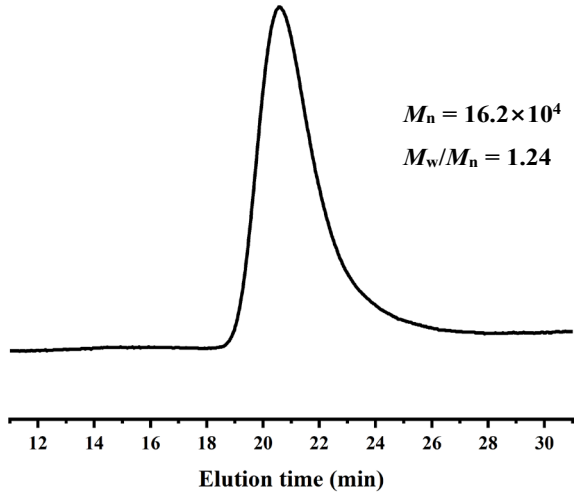

Figure S25. GPC curve of the 3,4-polyisorene from Entry 2 in Table 1.

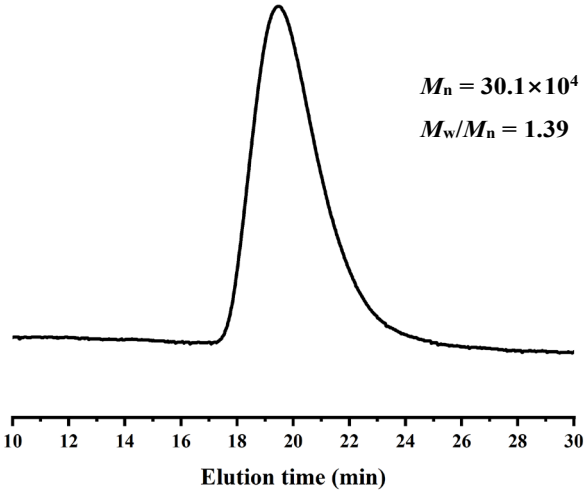

Figure S26. GPC curve of the 3,4-polymyrcene from Entry 1 in Table 2.

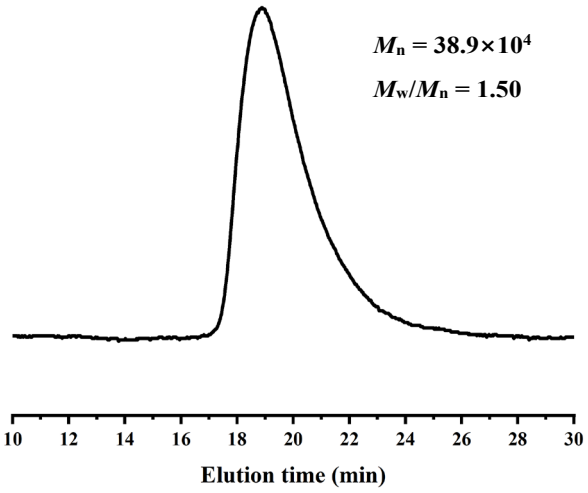

Figure S27. GPC curve of the 3,4-polyfarnesene from Entry 5 in Table 2.

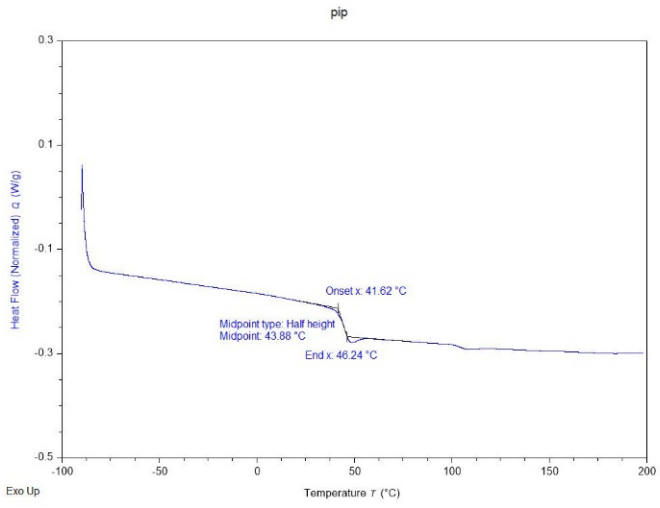

Figure S28. DSC chart of the 3,4-polyisorene (100%) from Entry 2 in Table 1.

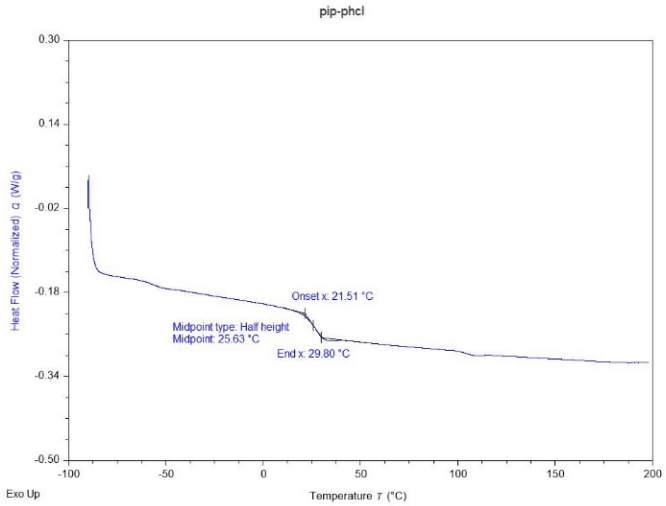

Figure S29. DSC chart of the 3,4-polyisorene (89.3%) from Entry 14 in Table 1.

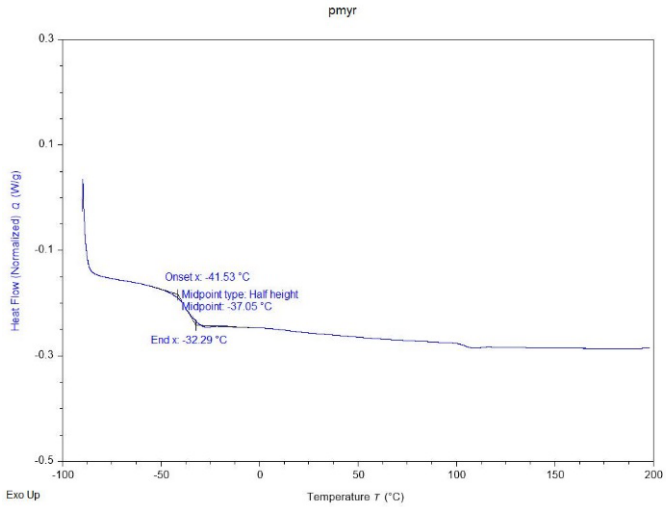

Figure S30. DSC chart of the 3,4-polymyrcene (100%) from entry 1 in Table 2.

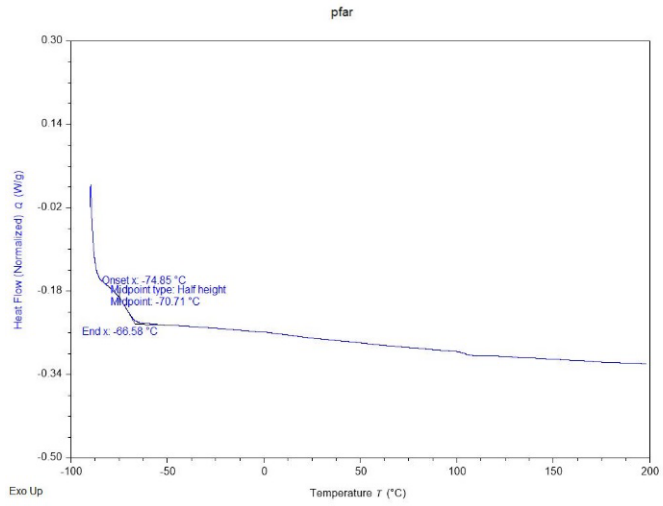

Figure S31 DSC chart of the 3,4-polyfarnesene (100%) from Entry 5 in Table 2.

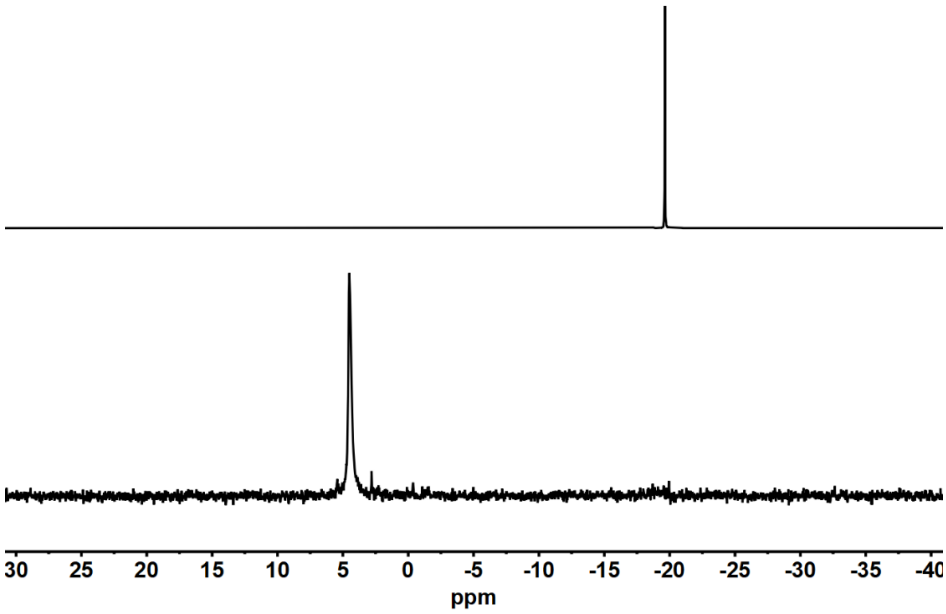

Figure S32 The ^{31}P NMR spectrum of monitoring the in situ reaction of the complex **P1-Lu** + $[Ph_3C][B(C_6F_5)_4]$. (400 MHz, C_6D_6, 25 °C)

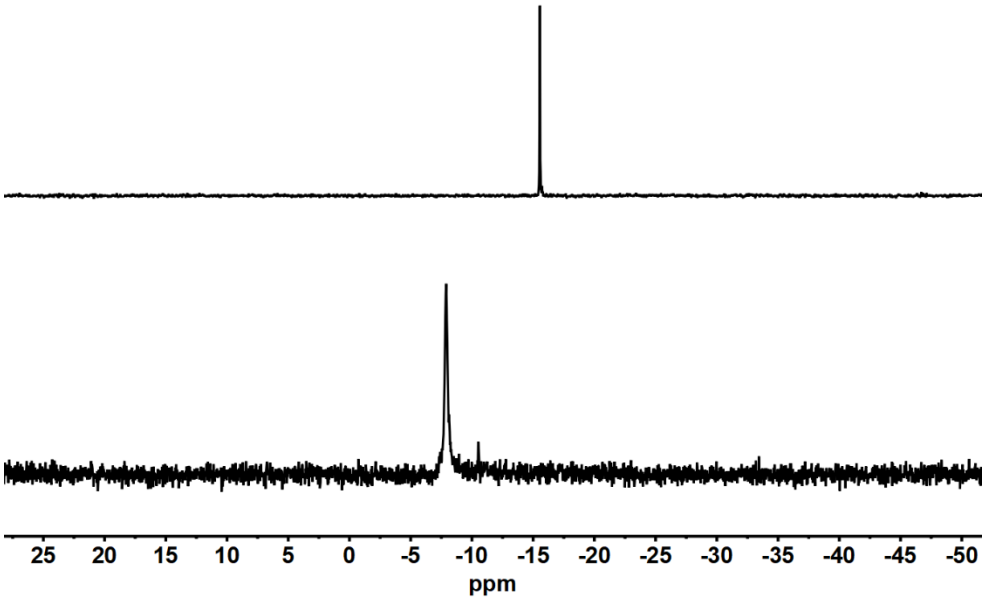

Figure S33 The ^{31}P NMR spectrum of monitoring the in situ reaction of the complex **P2-Sc** + $[Ph_3C][B(C_6F_5)_4]$. (400 MHz, C_6D_6, 25 °C)

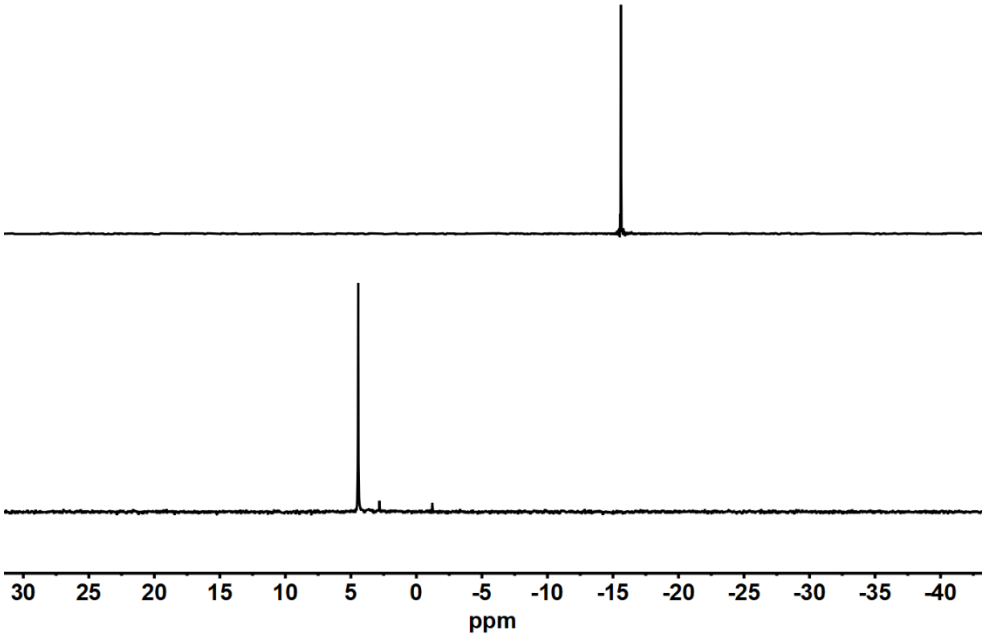

Figure S34 The ^{31}P NMR spectrum of monitoring the in situ reaction of the complex **P2-Lu** + $[Ph_3C][B(C_6F_5)_4]$. (400 MHz, C_6D_6, 25 °C)

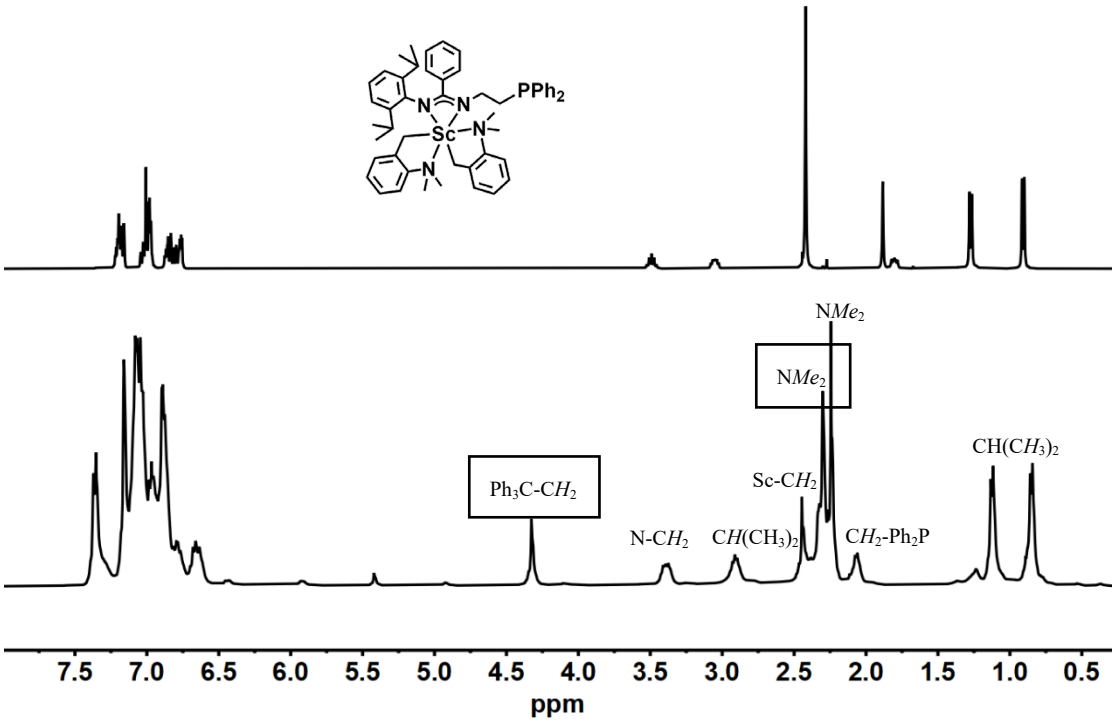

Figure S35 The ^{1}H NMR spectrum of monitoring the in situ reaction of the **P1-Sc** and $[Ph_3C][B(C_6F_5)_4]$ (400 MHz, C_6D_6, 25 °C).

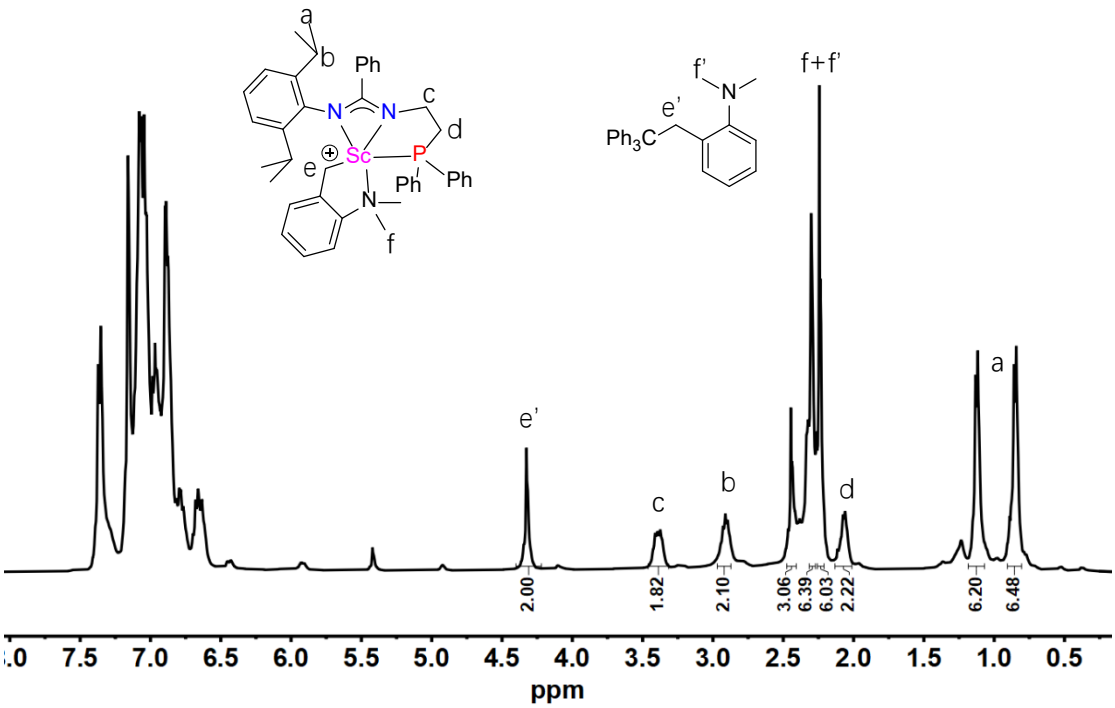

Figure S36 The ^{1}H NMR spectrum of the **P1-Sc**/[Ph_3C][$B(C_6F_5)_4$] (400 MHz, C_6D_6, 25 °C).

Table S2. Summary of the crystallographic data for **P1-Sc** and **P2-Sc**.

	P1-Sc	**P2-Sc**	[**L1**Sc($CH_2C_6H_4NMe_2$-*o*)$(THF)_2$][BPh_4]
Empirical formula	$C_{51}H_{58}N_4PSc$	$C_{52}H_{62}N_4PSc$, 0.35[C_6H_{14}], 0.275[C_6H_{14}]	$C_{50}H_{64}N_3O_2PSc$, $C_{24}H_{20}B$, 0.4[C_6H_{14}]
Formula weight	802.94	872.84	1168.65
Temperature/K	150(2)	150(2)	150.(2)
Wavelength/Å	0.71073	1.54178	0.71073
Crystal system	triclinic	triclinic	triclinic
Space group	P -1	P -1	P -1
a/Å	11.8185(12)	11.8911(6)	13.8049(4)
b/Å	12.4335(15)	15.1281(7)	37.9296(13)
c/Å	15.9472(17)	27.9116(14)	13.9080(5)
α/°	89.192(4)	93.267(3)	90
β/°	71.996(4)	90.002(4)	116.3810(10)
γ/°	87.743(4)	101.270(3)	90
V/Å^3	2226.9(4)	4915.9(4)	6524.0(4)
Z	2	4	4
D_c/Mg m^{-3}	1.197	1.179	1.190
μ/mm^{-1}	0.240	1.882	0.186
F(000)	856	1877	2504
Crystal size/mm^3	0.040 x 0.030 x 0.010	0.050 x 0.050 x 0.050	0.240 x 0.230 x 0.040
2θ range for data collection/°	1.89 to 25.15	1.58 to 66.85	1.96 to 24.71
Limiting indices(*hkl*)	-14,11;-14,14;-19,19	-14,14;-16,18;-33,33	-16,16;-44,44;-16,16
Reflections collected	13826	72491	172024
Independent reflections	7945	17382	22220
R_{int}	0.1220	0.1409	0.2226
Completeness to θ/°	25.15° (99.9%)	66.85° (99.5%)	24.71° (99.9%)
Data/restraints/parameters	7945/0/523	17382/0/1061	172024/1/1478
Goodness-of-fit on F^2	1.001	1.009	1.018
Final R indexes [I ≥ 2σ (I)]	R1 = 0.0574, wR2 = 0.1288	R1 = 0.0614, wR2 = 0.1677	R1 = 0.0574, wR2 = 0.1288
Final R indexes [all data]	R1 = 0.1831, wR2 = 0.2159	R1 = 0.0966, wR2 = 0.1481	R1 = 0.0972, wR2 = 0.1141
Largest diff. peak/hole/e Å^{-3}	0.633, -0.652	0.496, -0.548	0.500. -0.766

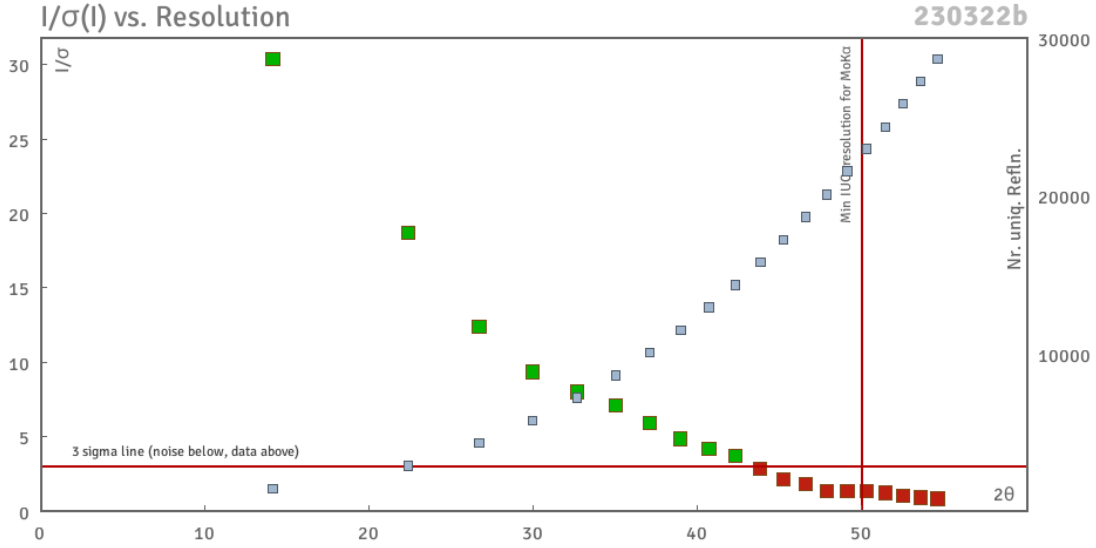

Figure S37 Plot of the signal to noise ratio I/σ(I) as a function of resolution based on crystallography of **P1-Sc**.

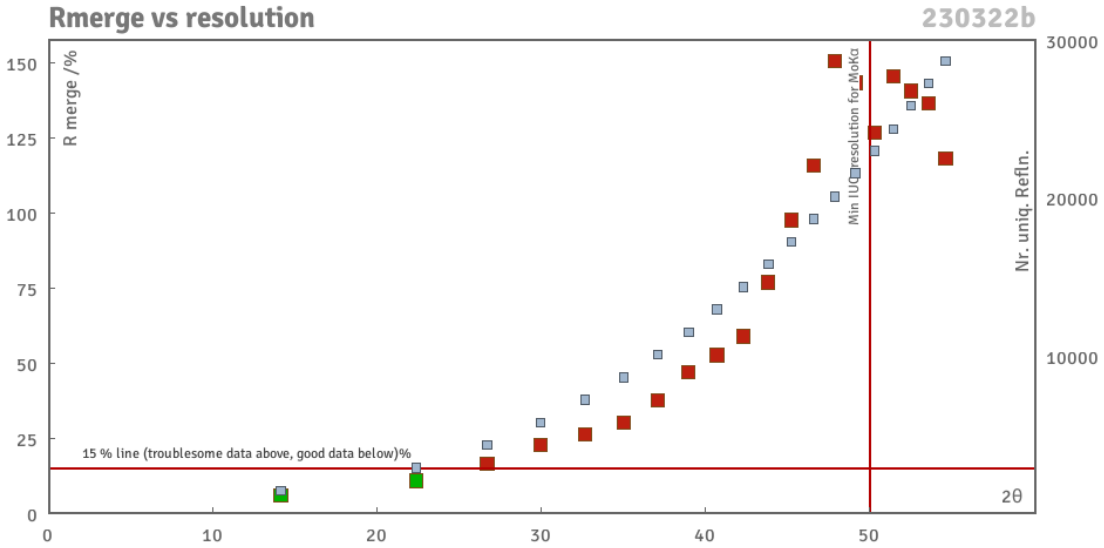

Figure S38 Rmerge as a function of resolution for **P1-Sc**.

Note: The crystal data in detail of **P1-Sc** (CCDC 2261242), was collected with a scan width of 1 degree and exposure time extended toof 10 seconds. The weak data for this structure might be attributed to the un-coordinated -PPh2 group that impeded the molecules to form well-assembly and compacted structure for X-ray diffraction analysis.

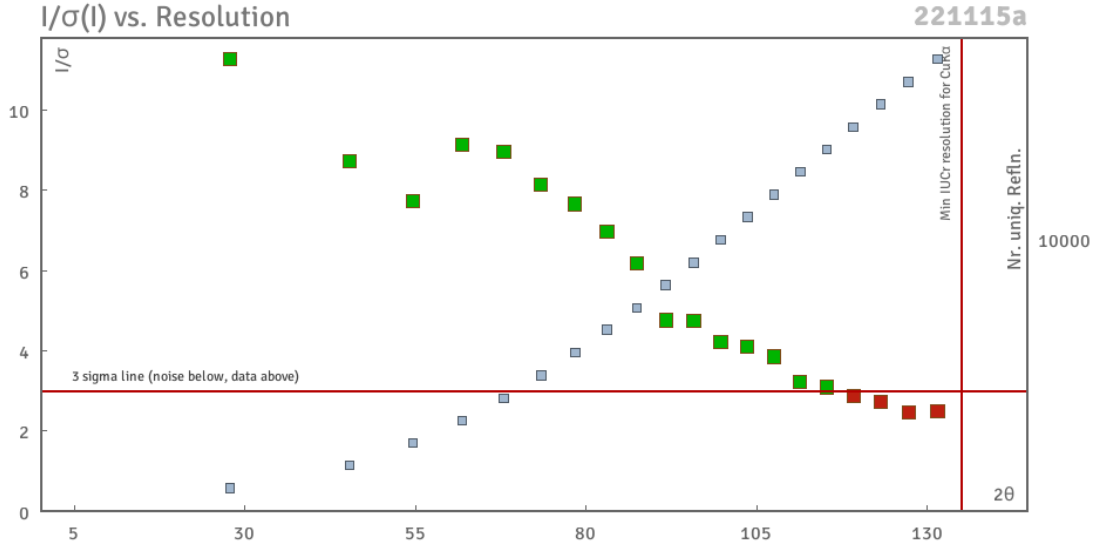

Figure S39 Plot of the signal to noise ratio I/σ(I) as a function of resolution based on crystallography of **P2-Sc**.

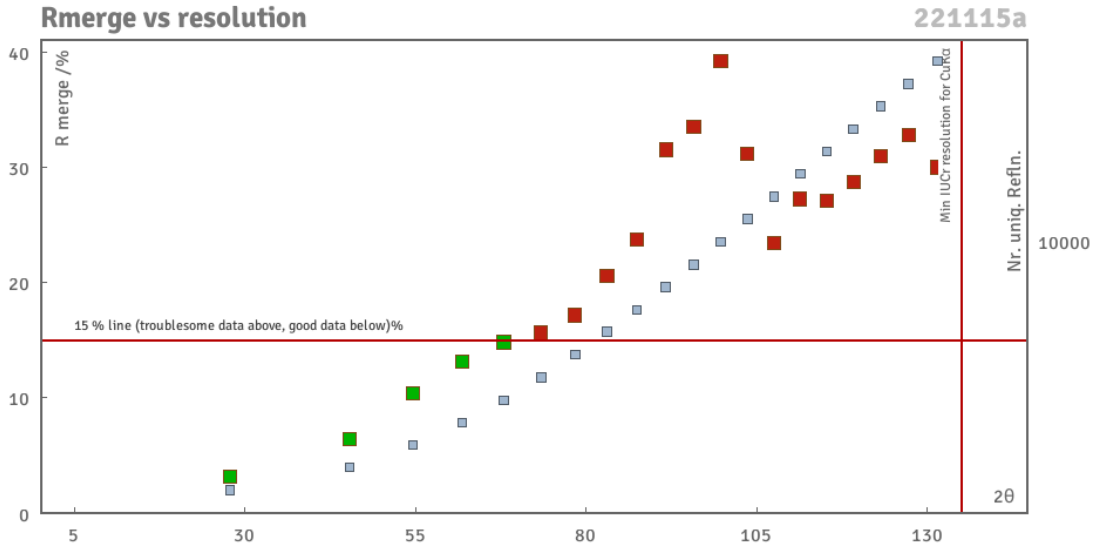

Figure S40 Rmerge as a function of resolution for **P2-Sc**.

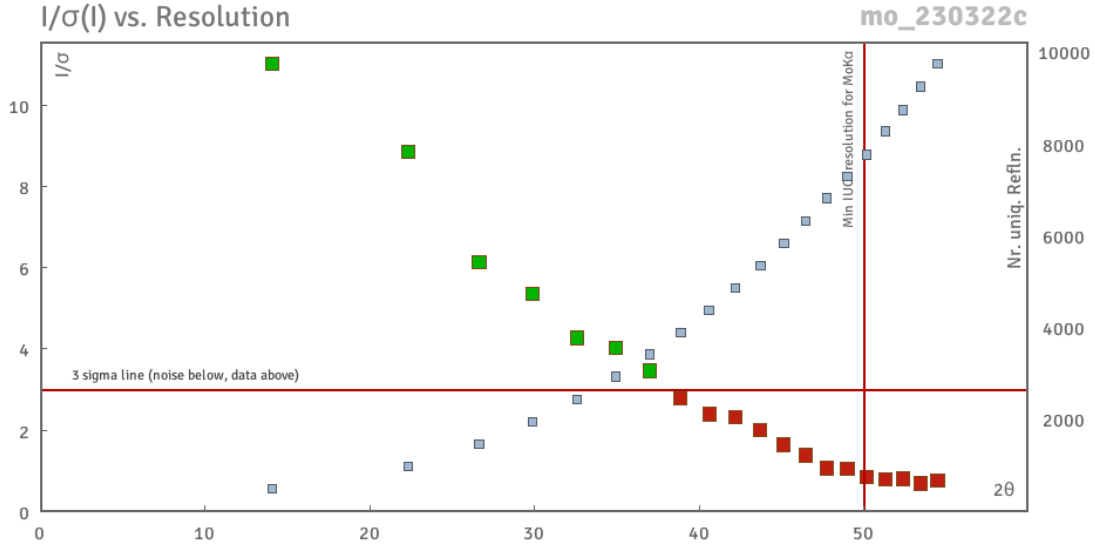

Figure S41 Plot of the signal to noise ratio I/σ(I) as a function of resolution based on crystallography of [**L1**Sc($CH_2C_6H_4NMe_2$-*o*)$(THF)_2$][BPh_4].

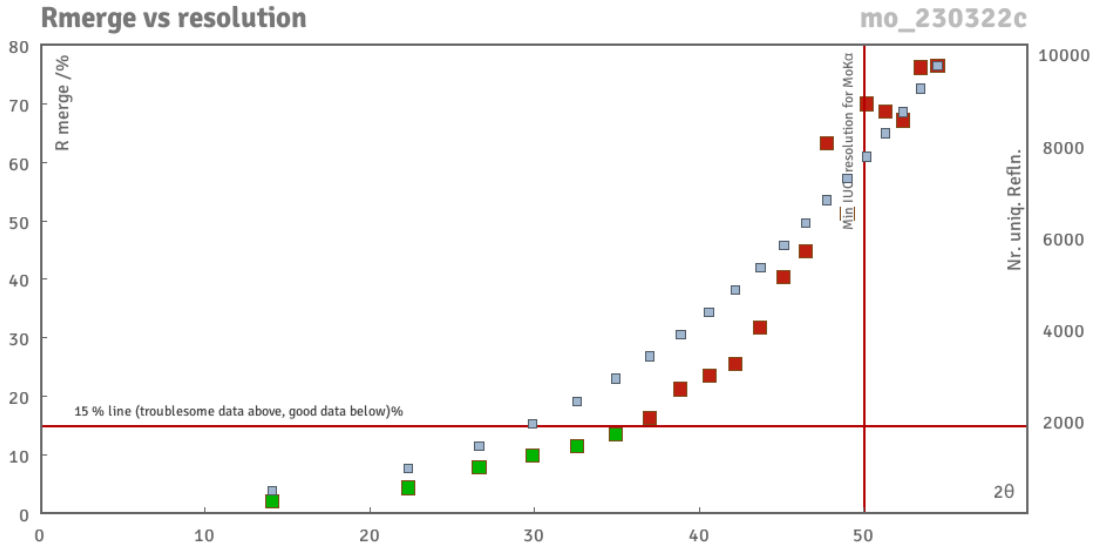

Figure S42 Rmerge as a function of resolution for [**L1**Sc($CH_2C_6H_4NMe_2$-*o*)$(THF)_2$][BPh_4].

Computational details

All calculations were performed with Gaussian 16 program.[1] The B3PW91 hybrid exchange-correlation functional was utilized for geometry optimization.[2-4] The 6-31G* basis set was considered for C, H, N, B, and F atoms, and the P and Sc atoms were treated by the Stuttgart/Dresden effective core potential (ECP) and the associated basis sets.[5,6] The basis sets of P were augmented with one *d*-polarization function (exponent of 0.387).[7] This basis set is denoted as "BSI". To obtain more reliable energy, the single-point calculations of optimized structures were carried out at the level of B3PW91-D3 (B3PW91 with Grimme's DFT-D3 correction)[8,9]/BSII, taking into account solvation effect of chlorobenzene with the SMD[10] solvation model. In the BSII, the 6-311G(d,p) basis set was used for nonmetal atoms, while the basis sets together with associated pseudopotentials for Sc atom are the same as that in geometry optimization.

(1) Frisch, M. J. T.; G. W.; Schlegel, H. B.; Scuseria, G. E.; Robb, M. A.; Cheeseman, J. R.; Scalmani, G.; Barone, V.; Mennucci, B.; Petersson, G. A.; Nakatsuji, H.; Caricato, M.; Li, X.; Hratchian, H. P.; Izmaylov, A. F.; Bloino, J.; Zheng, G.; Sonnenberg, J. L.; Hada, M.; Ehara, M.; Toyota, K.; Fukuda, R.; Hasegawa, J.; Ishida, M.; Nakajima, T.; Honda, Y.; Kitao, O.; Nakai, H.; Vreven, T.; Montgomery, J. A., Jr.; Peralta, J. E.; Ogliaro, F.; Bearpark, M.; Heyd, J. J.; Brothers, E.; Kudin, K. N.; Staroverov, V. N.; Kobayashi, R.; Normand, J.; Raghavachari, K.; Rendell, A.; Burant, J. C.; Iyengar, S. S.; Tomasi, J.; Cossi, M.; Rega, N.; Millam, N. J.; Klene, M.; Knox, J. E.; Cross, J. B.; Bakken, V.; Adamo, C.; Jaramillo, J.; Gomperts, R.; Stratmann, R. E.; Yazyev, O.; Austin, A. J.; Cammi, R.; Pomelli, C.; Ochterski, J. W.; Martin, R. L.; Morokuma, K.; Zakrzewski, V. G.; Voth, G. A.; Salvador, P.; Dannenberg, J. J.; Dapprich, S.; Daniels, A. D.; Farkas, Ö.; Foresman, J. B.; Ortiz, J. V.; Cioslowski, J.; Fox, D. J. *Gaussian 16, Revision C.01*; Gaussian, Inc.: Wallingford, CT,. **2016**.

(2) Becke, A. Density-functional thermochemistry. III. The role of exact exchange. *J. Chem. Phys.* **1993**, *98*, 5648–5653.

(3) Lee, C.; Yang, W.; Parr, R. Development of the Colic-Salvetti correlation-energy formula into a functional of the electron density. *Phys. Rev. B* **1988**, *37*, 785−789.

(4) Perdew, J.; Burke, K.; Wang, Y. Generalized gradient approximation for the exchange-correlation hole of a many-electron system. *Phys. Rev. B* **1996**, *54*, 16533−16539.

(5) Andrae, D.; H. U.; Dolg, M.; Stoll, H.; P, H. Energy-adjusted Ab initio pseudopotentials for the second and third row transition elements. *Theor. Chim. Acta* **1990**, *77*, 123−141.

(6) Martin, J.; Sundermann, A. Correlation consistent valence basis sets for use with the Stuttgart-Dresden-Bonn relativistic effective core potentials: The atoms Ga-Kr and In-Xe. *J. Chem. Phys.* **2001**, *114*, 3408−3420.

(7) Höllwarth, A.; Böhme, M.; Dapprich, S.; Ehlers, A. W.; Gobbi, A.; Jonas, V.; Köhler, K. F.; Stegmann, R.; Veldkamp, A.; Frenking, G. A set of d-polarization functions for pseudo-potential basis sets of the main group elements Al-Bi and f-type polarization functions for Zn, Cd, Hg, *Chem. Phys. Lett.* **1993**, *208*, 237–240.

(8) Grimme, S.; Antony, J.; Ehrlich, S.; Krieg, H. A consistent and accurate ab initio parametrization of density functional dispersion correction (DFT-D) for the 94 elements H-Pu. *J.*

Chem. Phys. **2010**, *132*, 154104–15424.

(9) Grimme, S. Accurate description of van der waals complexes by density functional theory including empirical corrections. *J. Comput. Chem.* **2004**, *25*, 1463–1473.

(10) Marenich, A.; Cramer, C.; Truhlar, D. Universal solvation model based on solute electron density and on a continuum model of the solvent defined by the bulk dielectric constant and atomic surface tensions. *J. Phys. Chem. B.* **2009**, *113*, 6378–6396.

Note after first publication:
This Electronic Supplementary Information replaces the version first published on 17 Jun 2023. The crystal structure data has been updated, and additional discussion of the crystal structure data has been added to this ESI document.